Applied Thermal Engineering 181 (2020) 115592

Contents lists available at ScienceDirect

Applied Thermal Engineering

journal homepage: www.elsevier.com/locate/apthermeng

Multi-objective optimization of a hybrid microchannel heat sink combining manifold concept with secondary channels

Min Yang, Bing-Yang Cao*

Key Laboratory for Thermal Science and Power Engineering of Ministry of Education, Department of Engineering Mechanics, Tsinghua University, Beijing 100084, PR China

HIGHLIGHTS

- A novel optimization approach is proposed to optimize the performance of a hybrid heat sink.
- The Pareto-optimal set is obtained and verified by CFD results.
- The optimized heat sink can reduce thermal resistance by 18.83% compared with manifold heat sink.
- TOPSIS with entropy weight method is applied to select the best compromise solution from Pareto-optimal set.

ARTICLE INFO

Keywords:
Microchannel heat sink
Hybrid design
Multi-objective optimization
Design of experiment
Response surface methodology
Pareto-optimal solution

ABSTRACT

A novel optimization approach, which combines optimal Latin hypercube design (Opt LHD), Pareto chart analysis, response surface methodology (RSM), the non-dominated sorting genetic algorithm II (NSGA-II) and technique for order preference by similarity ideal solution (TOPSIS), has been proposed and applied to optimize the performance of a hybrid microchannel heat sink combining manifold concept with secondary oblique channels. Four geometric parameters are selected as design variables and the optimization objective is to minimize the total thermal resistance R_t and pumping power P_p simultaneously. First, 160 sample points is generated by Opt LHD and the Pareto chart analysis is performed to identify the dominant design parameters influencing the objectives. Then, RSM is used to generate approximate models relating to the objectives and design parameters, and NSGA-II is selected to minimize R_t and P_p. 374 Pareto-optimal solutions are obtained and verified by CFD results, which indicates that the hybrid design can reduce R_t by 18.83% compared with manifold microchannel heat sink under the same P_p. Finally, the best compromise solution is obtained by TOPSIS combined with entropy weight method. The proposed optimization approach can also be applied to optimize the performance of other types of heat sinks.

1. Introduction

Gordon Moore predicted that the number of incorporated transistors in a chip would approximately double every 18 months to two years in 1965, a growth trend known as Moore's law [1], which was confirmed by subsequent industrial development [2]. Today, one processor has billions of transistors in about 1 cm^2 chip and the heat flux exceeds 100 W/cm^2 [3]. In addition, the rapid development of 3D integrated circuit based on through-silicon via (TSV) technology further increases the packaging density. The heat flux to be dissipated in next-generation electronic devices will exceed 1000 W/cm^2 [4]. The failure of removing the high heat flux will increase the temperature of electronics significantly, which will damage the electronic devices [5,6]. Therefore, it is necessary to take the thermal management into account during the design of various electronic devices. Liquid cooling strategy [7–9] is becoming more important in the thermal management of electronic systems with high heat flux because of the low thermal conductivity of air [10,11]. In 1981, Tuckerman and Pease [12] proposed microchannel heat sink firstly and confirmed that it could remove heat flux as high as 790 W/cm^2 by experimental research. However, the required pressure loss was up to 214 kPa, which brings a serious challenge to the driven pump design. Because of its combined benefits of large surface-to-volume ratio and entrance effect, the microchannel heat sink has high heat removal capability and is considered to be the most promising cooling strategy for thermal management of electronic devices [13]. Research always focuses on the influence of microchannel shape,

* Corresponding author.
E-mail address: caoby@tsinghua.edu.cn (B.-Y. Cao).

https://doi.org/10.1016/j.applthermaleng.2020.115592
Received 7 February 2020; Received in revised form 20 April 2020; Accepted 9 June 2020
Available online 16 June 2020

Nomenclature

A_{hs}	heat source area (m^2)
d	secondary channel width (m)
H_b	base height (m)
H_c	channel height (m)
$H_{i\text{-}o}$	inlet/outlet height (m)
L_c	total channel length (m)
P_p	pumping power (W)
ΔP	pressure drop (Pa)
q''	heat flux (W/m^2)
Q	total heat flux (W)
R	thermal resistance (K/W)
T	Temperature (K)
q_v	volume flow rate (m^3/s)
w	attribute weight
W_c	channel width (m)
W_w	channel wall width (m)
W_{in}	manifold inlet width (m)
W_{out}	manifold outlet width (m)

Subscripts

c	channel
CFD	Computational Fluid Dynamics
in	inlet
out	outlet
Pre	prediction
r	ration
t	total
w	wall

physical parameters of cooling medium, wall roughness and other factors on the flow and heat transfer characteristics in the early stage limited by simulation method and micromachining technology [14–17]. However, due to the continuous heat absorption of the coolant in the microchannel, the thermal boundary layer gradually develops along the flow direction, which will increase the fluid temperature and temperature difference within the heat sink. In addition, the technology progress leads to higher heat flux density in modern electronic devices, which makes the microchannel heat sink with simple structure far from meeting the heat dissipation demand. There is an urgent need to develop new technology and structure to improve the overall performance of microchannel heat sink [18,19]. Because passive strategies of convective heat transfer enhancement only increase heat exchange by optimizing channel structure and does not need additional equipment or energy, which has attracted extensive attention.

With the development of simulation method and micromachining technology, many passive strategies have been studied, such as microchannel heat sink with wavy channel [20,21], cavities or pin fins [22–25], double-layer microchannel heat sink [26,27], manifold microchannel heat sink [28–35] and secondary flow [36–39]. These improved channel structures can increase the convective heat exchange area, periodically destroy the flow and thermal boundary layer, strengthen the mixing between the fluid in the wall region and the central region, it is to say that optimizing the synergy degree between velocity and temperature fields [40,41], so as to obtain better heat transfer performance. It is important to point out that secondary flow and manifold microchannel heat sink are two of the most important passive cooling strategies. A traditional microchannel (TMC) heat sink contains one inlet locating at one side of the device and one outlet locating at the opposite side. Unlike TMC heat sink, the manifold microchannel (MMC) heat sink has coolant distribution manifolds, which can form alternating inlet and outlet channels. During cooling operation, the working liquid flows normal to the fins and heat source guided by manifolds, which can greatly reduce the pressure loss due to the significant decrease in flow length. The hydraulic and thermal performance of manifold heat sink has been studied extensively [28–35]. Secondary flow is another effective passive chip-cooling technique. Smaller cooling channels, i.e. secondary channels, are created by offset strip fins and can generate secondary flow, which can enhance heat transfer by generating vortex and thinning the thermal boundary layer. It should be noted that the extra pressure drop caused by secondary flow is the limiting factor if the geometric parameters are not designed properly [36–39].

However, simple passive enhancement strategy can no longer meet the rapid growth of heat dissipation demand, so it is necessary to integrate the advantages of various structures. Therefore, we have proposed a novel cooling scheme combining manifold with secondary oblique channels (MMC-SOC) [42]. The manifold structure is able to reduce pressure drop by reducing the flow length in microchannels and the secondary channels can enhance the heat transfer by combined benefits of fluid mixing and boundary layer re-development. Fig. 1 is a schematic diagram of the hybrid MMC-SOC heat sink concept. Figs. 1(a) and (b) are three-dimensional view and top view of the hybrid microchannel heat sink respectively. The whole structure can be divided into two layers, the upper layer is the coolant distribution manifold structure and the lower layer is embedded microchannel heat sink, including chip and microchannel structure. It can be seen from Fig. 1(a) that when the coolant flows along the inlet formed by the manifold structure, it will cool the fins under the inlet in the way of impinging jet. In addition, the original straight rib is broken into trapezoidal ribs to form discontinuous microchannels. It can be seen in Fig. 1(b) that some of the coolant flows into the secondary channels formed by the discontinuous rib when the coolant flows along the main channel, which can enhance the flow disturbance. Our simulation results [42] have indicated that MMC-SOC heat sink could reduce the pressure loss and heat source temperature simultaneously compared with MMC heat sink. In addition, the parameters had great influence on the MMC-SOC heat

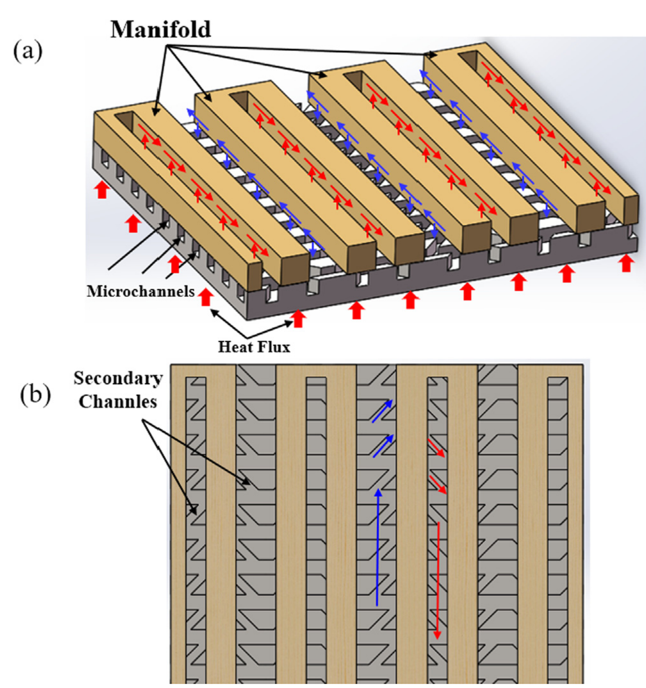

Fig. 1. Hybrid microchannel heat sink: (a) partial 3-D view, and (b) plan view.

sink performance and it is necessary to carry out reasonable design optimization.

In order to guide the geometric design of MMC-SOC heat sink, this paper employs multi-objective evolutionary algorithm [43–46] to minimize the total thermal resistance R_t and pumping power P_p simultaneously by optimizing the main structure parameters of the hybrid heat sink. A novel optimization approach combining optimal Latin hypercube design (Opt LHD), Pareto chart analysis, response surface methodology (RSM), the non-dominated sorting genetic algorithm II (NSGA-II) and technique for order preference by similarity ideal solution (TOPSIS) has been proposed. The relative secondary channel width d_r, relative longer-edge length W_{1r} of the fin under the inlet, relative channel width W_{cr} and relative channel wall width W_{wr} are selected as four dimensionless optimization variables. Minimizing the total thermal resistance R_t and pumping power P_p meanwhile under constant water flow rate is the optimization objective. To ensure that all designs are well spread over the design space, a design matrix with 160 sample points are generated by Opt LHD. The Pareto chart analysis is performed to identify the dominant design parameters influencing the optimization objective. Approximate models between the objectives and design parameters are generated by RSM and NSGA-II is selected to minimize P_p and R_t. 374 Pareto-optimal solutions are obtained and verified by CFD results. Compared with a simple MMC heat sink, the optimal hybrid heat sink can reduce R_t by 18.83% under the same P_p. Finally, TOPSIS combined with entropy weight method is used to obtain the best compromise solution from the Pareto-optimal set.

2. Hybrid microchannel heat sink

2.1. Modeling

As illustrated in Fig. 2, an entire computational domain with one inlet and two outlets is taken from the hybrid microchannel heat sink. A total of ten microchannels is etched in the back of a 400 μm-thick silicon substrate. Two manifold outlets are located at both ends of the heat sink and one manifold inlet is located between the two outlets. The widths of manifold outlet W_{out} and inlet W_{in} are 0.8 mm and 1.6 mm, respectively. The longer-edge length W_2 of the fin except those under the inlet is 500 μm. The heights of the inlet/outlet and base are $H_{i\text{-}o} = 300$ μm and $H_b = 100$ μm, respectively. The microchannel height H_c and total channel length L_c are 300 μm and 10.6 mm, respectively. It is clear that there is a symmetry between left and right halves of the entire computational domain and half of it can model the thermal and flow characteristics of the MMC-SOC heat sink. Therefore, we only carry out simulation and optimization studies on half of the entire computational domain. A laminar model is applied in our study because that the Reynolds number ranges from 177 to 442. It should be pointed out that the current study applies the same numerical method, including the governing equations, boundary conditions, grid independence test, validation of the numerical results, etc., as in our previous study [42].

2.2. Design variables and optimization objectives

As for microchannel, the channel height H_c, width W_c and wall width W_w all have significant effects on the heat sink performance. Our previous study [42] has indicated that the secondary channel width d and the longer-edge length W_1 of the trapezoid fin are two important parameters. As for manifold microchannel heat sink, previous studies [33,42] have indicated that both the manifold and microchannel sections must be considered simultaneously. Therefore the manifold inlet width W_{in} is chosen to optimize. Here, the secondary channel width d, the channel width W_C, the channel wall width W_w and the longer-edge length W_1 of the fin under the inlet are chosen as optimization variables. Four dimensionless design variables are also defined based on those geometric parameters, i.e. the relative secondary channel width ($d_r = d/W_c$), the relative longer-edge length ($W_{1r} = W_1/W_{in}$), the relative channel width ($W_{cr} = W_c/H_c$) and the relative channel wall width ($W_{wr} = W_w/W_c$). The variation ranges of these four dimensionless design variables are as follows: $d_r \in [0.2, 2.5]$, $W_{1r} \in [0.2, 2.5]$, $W_{cr} \in [0.25, 1]$ and $W_{wr} \in [0.5, 1.2]$. It should be noted that the variation range should be as large as possible, so that the optimization can be performed in a larger space. In addition, the variation range should ensure successful modeling and manufacturing. The minimum value of those four optimization variables is $d_{min} = 15$ μm, which is selected based on the manufacturing limitation. Besides, the total flow length is 5.3 mm and we hope that there are at least two trapezoid fins to decrease the heat source temperature, one under the inlet and the other near the outlet. Therefore, the maximum values of the secondary channel width and the longer-edge length of the fin under the inlet are designed as $d_{max} = 750$ μm and $W_{1,\ max} = 4$ mm. In the optimization process, the total thermal resistance R_t and pumping power P_p of the hybrid microchannel heat sink are selected as objective functions. The total thermal resistance R_t is defined as

$$R\ t = \frac{\Delta T_{max}}{Q} = \frac{T_{max} - T_{in}}{Q}, \tag{1}$$

where T_{max} is the maximum temperature of the heat source and T_{in} is the inlet fluid temperature. Q is the applied heating power and is the product of the heat flux q'' and heating area A_{hs}, i.e.

$$Q = q'' \times A_{hs}. \tag{2}$$

The pumping power P_p is expressed as

$$P_p = \Delta P \times q_v, \tag{3}$$

where ΔP and q_v are the pressure drop and volume flow rate, respectively. The total thermal resistance R_t and pumping power P_p are simultaneously minimized at constant volume flow rate in the optimization process.

3. Optimization procedures

The entire multi-objective optimization flow chart is presented in Fig. 3. The optimization procedure steps are as follows:

(1) Determine the design variables with corresponding design space, and objective functions;
(2) Use the design of experiment (DOE) to obtain sample points in the

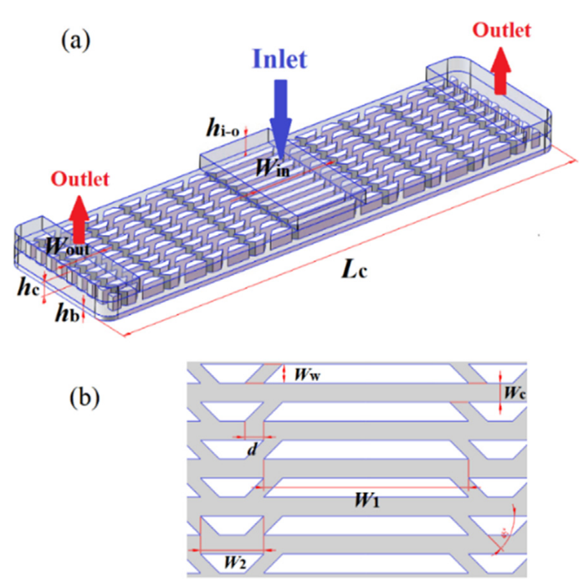

Fig. 2. (a) Schematic diagram and (b) geometric parameters of the MMC-SOC heat sink.

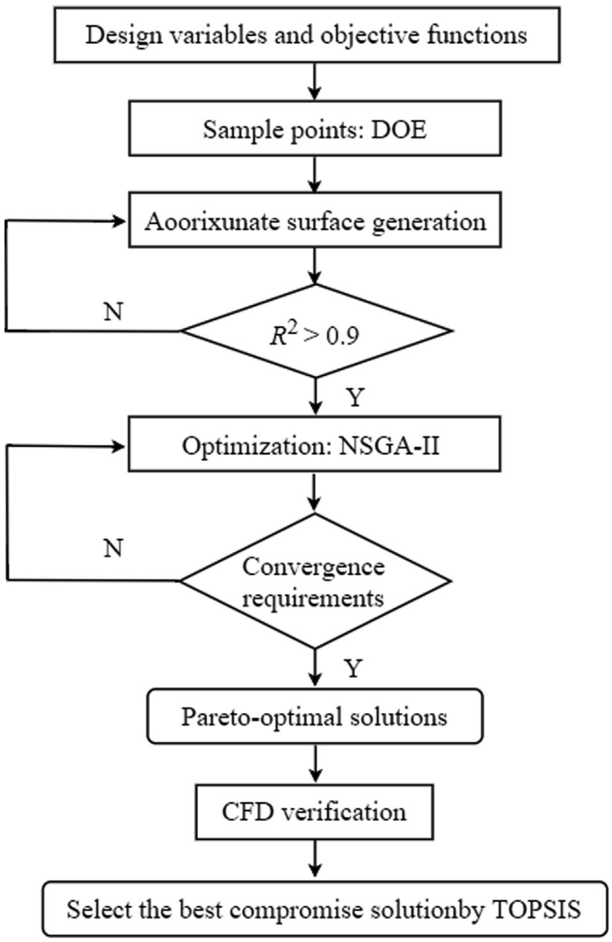

Fig. 3. Multi-objective optimization workflow chart.

design space and then obtain the initial sample data points through numerical simulation;

(3) Construct the approximate model between design variables and objective functions according to the initial sample points by using RSM;
(4) Obtain the Pareto-optimal solutions based on the multi-objective genetic algorithm and compare these predictions with the CFD results to ensure the accuracy of the predicted values;
(5) Finally, TOPSIS combined with entropy weight method is used to choose the best compromise solution (BCS) from Pareto-optimal solutions.

3.1. Design of experiment

The location of the evaluation data points in design space used for generating response surface is essential for RSM. The methodology used for formulating the plan data points in design space is collectively known as DOE, which is able to reflects the characteristics of design space based on a small amount of data points. In the present study, Opt LHD is used to obtain the plan data points in design space. Opt LHD [47] can ensure the distribution uniformity of the sample points through combination optimization. A total of 160 sample points is generated by the Opt LHD method.

3.2. Response surface methodology

Approximate model revealing the relationship between the input parameters and output responses should be constructed according to the initial data points before the optimization of the geometric parameters. The accuracy of approximate model significantly influences the optimization results. In this study, two responses, i.e. the total thermal resistance R_t and pumping power P_p, are selected as the objective functions and every response is influenced by four input variables. In order to construct the approximate model between the design variables and objective functions, RSM is used in this study. RSM, proposed by Box and Wilson [48], contains a collection of mathematical and statistical techniques that can be used to analyze those optimization problems with several input variables and output responses [49]. The main advantage of RSM is its ability to exhibit the factor contributions based on reduced number of required data points. In this study, a third-order polynomial function is used to generate the mathematical model between the response and the input and it can be expressed as follows:

$$\tilde{y} = \beta_0 + \sum \beta_i x_i + \sum \beta_{ii} x_i^2 + \sum \beta_{iii} x_i^3 + \sum_{i \neq j} \beta_{ij} x_i x_j, \tag{4}$$

where y is the fitted value of the model, x_i and x_j are the input variables. β_O, β_i, β_{ii}, β_{iii} and β_{ij} are the constant, linear, quadratic, cubic and interaction terms, respectively. It's necessary to check whether the model fits the numerical data well after building the response surface model. Generally, the coefficient of multiple determination (R^2) can be used to evaluate the predictive capability of the model:

$$R^2 = \frac{SST - SSE}{SST} = \frac{\sum (y_i - \bar{y})^2 - \sum (y_i - \tilde{y}_i)^2}{\sum (y_i - \bar{y})^2}, \tag{5}$$

where SST is the sum of squares for total, SSE is the sum of squares for error, $\bar{y}$ is the mean value of corresponding y and y is the response value of the approximate model. In general, a larger value of R^2 always means a higher credibility of the model and R^2 value is generally required to be larger than 0.9.

3.3. Multi-objective optimization algorithm

In both scientific research and engineering practice, there are many problems of optimizing multiple objectives at the same time, which are collectively called multi-objective optimization problem (MOP). In MOP, objectives are often in conflict with each other. When one objective is improved, some others may degrade. Therefore, it is impossible to make all objectives reach the optimum solution meanwhile. A solution is called Pareto-optimal solution if no other solutions superior to it can be found in the design space when all optimization objectives are considered. In MOP, there is no single optimal solution, but rather a set of solutions composed of multiple or even infinite Pareto-optimal solutions. Generally, the multi-objective optimization problem can be described as follows:

$$\begin{aligned}
&\text{Min(\&Max)}\ \ \boldsymbol{y} = \boldsymbol{F}(\boldsymbol{x}) = (f_1(\boldsymbol{x}), f_2(\boldsymbol{x}), \text{Â·Â·Â·} f_m(\boldsymbol{x})),\\
&\text{S. t.}\quad g_i(\boldsymbol{x}) \le 0,\ i = 1, 2, \text{Â·Â·Â·}p\\
&h_i(\boldsymbol{x}) = 0,\ j = 1, 2, \text{Â·Â·Â·}q\\
&\boldsymbol{x} = (x_1, x_2, \text{Â·Â·Â·}x_n) \in \boldsymbol{X} \subset R^{\mathrm{n}}\\
&\boldsymbol{y} = (y_1, y_2, \text{Â·Â·Â·}y_m) \in \boldsymbol{Y} \subset R^{\mathrm{m}},
\end{aligned} \tag{6}$$

where m and n are the number of objectives and optimization variables, respectively. p and q are the number of inequality and equality constraints, respectively. $\boldsymbol{X}$ is the feasible decision space formed by the decision vector $\boldsymbol{x}$ and $\boldsymbol{Y}$ is the goal space formed by the goal vector $\boldsymbol{y}$. $g_i(x)$ and $h_i(x)$ are inequality and equality constraints, respectively. NSGA-II is selected to solve the RSM model established in the previous section. In 2002, Deb et al. [50] proposed the NSGA-II algorithm and their simulation results have proved that the NSGA-II algorithm is an efficient and effective technique to solve the multi-objective problems. The basic principle of NSGA-II algorithm can be divided into three key steps: Firstly, the initial population is generated at random, and then three basic operations, i.e. selection, crossover and variation, are performed according to a certain probability after non-dominated sorting to obtain the first-generation population. Secondly, a fast non-dominated sorting is made by combining the parent population with offspring population together from the second-generation. Meanwhile, the crowding degree of each individual in each non-dominated layer is calculated. Then, those appropriate individuals are selected to form a new parent population based on the non-dominated relationship and the crowding degree of each individual. Finally, a new generation population is generated by the basic operation of genetic algorithm until the conditions for the end of the program are met. It should be noted that a Pareto-optimal solution obtained by using NSGA-II may not be the optimal solution of other optimization strategies.

3.4. TOPSIS

Selecting a relative optimal scheme from available alternatives, and each of which has multiple attributes, is referred to as a multi-attribute decision making (MADM) problem. For Pareto-optimal solutions obtained in this paper, each solution has two attributes, i.e. the pumping power P_p and total thermal resistance R_t. Therefore, selecting the relative optimal solution from Pareto-optimal solutions is a typical MADM problem. However, we cannot simply select the best solution according to only their pumping power or thermal resistance because every solution is the best structure under the corresponding working condition. Therefore, we choose TOPSIS method to select the best compromise solution. TOPSIS is based on the primary principle that the chosen alternative solution should have the "farthest distance" from the negative-ideal solution and the "shortest distance" from the positive-ideal solution [51]. For MADM, determining attribute weights is crucial to measure the relative importance in decision making process. Subjective and objective methods are two widely used weighting methods. The subjective method determines attribute weights by the preference or experience of decision makers. By contrast, the objective method determines attribute weights according to mathematical models without considering the subjective judgement information of decision makers, for example, the information entropy weight method. Therefore, in order to objectively evaluate the Pareto-optimal solutions, we attempt to apply the information entropy weight to obtain the attribute weights and use the TOPSIS method to select the best compromise solution.

4. Results and discussion

4.1. Sensitivity analysis

Sensitivity analysis, which can identify the effects of various input parameters on objectives, is increasingly being considered as essential for good modeling practice. Parameters with higher sensitivity coefficients are more important for modeling while those with much lower coefficients can be neglected. Our previous simulation results [42] have indicated that there is no definite relationship between the thermal resistance and d_r, or the pressure drop and d_r. Therefore, a statistical sensitivity analysis methodology named Pareto chart analysis is chosen to quantitatively describe the effects of these four geometric parameters on the optimization objectives. Pareto chart analysis is a widely used approach in engineering applications to identify the most frequent defects, complaints, or any other factors. A design matrix with 160 sample points is generated by Opt LHD. According to the geometric parameters of those sample points, UG is used to construct CAD model by parametric modeling, and then three dimensional polyhedral mesh is generated by STAR-CCM+. The heat transfer and flow equations are solved by ANSYS Fluent 14.0 at a water volume flow rate of 0.08 L/min. The above operations are integrated by using a software platform (e.g. ISIGHT), and can be performed automatically, which improves the optimization efficiency greatly. Fig. 4 shows the Pareto charts of P_{in} and T_{max} based on the 160 sample points, where the abscissa is the percentage of influence and the ordinate is four dimensionless design parameters. The negative number represents a negative effect, while the positive number represents a positive effect. Figs. 4(a) and (b) show the effects of four geometric parameters on the inlet pressure P_{in} and the maximum temperature T_{max} of the heat source, respectively. It can be seen that:

(1) Whether for P_{in} or T_{max}, the design parameters W_{cr} has the most significant effects and the effect degrees reach up to −77.69% and 79.12% respectively. Increasing W_{cr} would decrease P_{in} and increase T_{max};
(2) For P_{in}, the effect of W_{wr} is smaller than W_{cr} but larger than W_{1r}. In addition, the design parameter d_r has a negligible effect degree of −0.08% on P_{in};
(3) For T_{max}, the effect of d_r is smaller than W_{cr} but larger than W_{1r}. In addition, the design parameter W_{wr} has a negligible effect degree of −0.6% on T_{max};
(4) Besides, whether for P_{in} or T_{max}, the design parameter W_{1r} has similar positive effect degree and the effect degrees are 6.77% and 2.91% respectively.

The above analyses indicate that, in order to reduce the time and cost in building approximate model between input parameters and objectives, the effect of d_r on P_{in} and the effect of W_{wr} on T_{max} can be ignored.

The temperature, pressure contours and the flow velocity, streamline distributions are analyzed at the same flow rate (0.08 L/min) to show the effects of design variables d_r and W_{wr} on the objective functions before optimization. Fig. 5 displays the temperature and pressure distribution contours for heat sinks with d_r = 1.0, and d_r = 1.5 when other design variables are kept constant (W_{1r} = 1.008, W_{cr} = 0.5 and

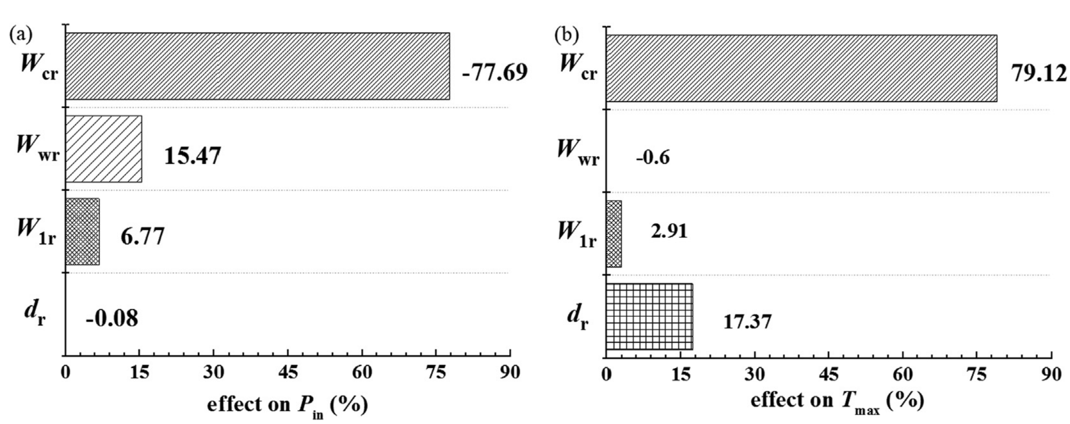

Fig. 4. Effects of geometric parameters on (a) inlet pressure P_{in} and (b) maximum temperature T_{max} of heat source.

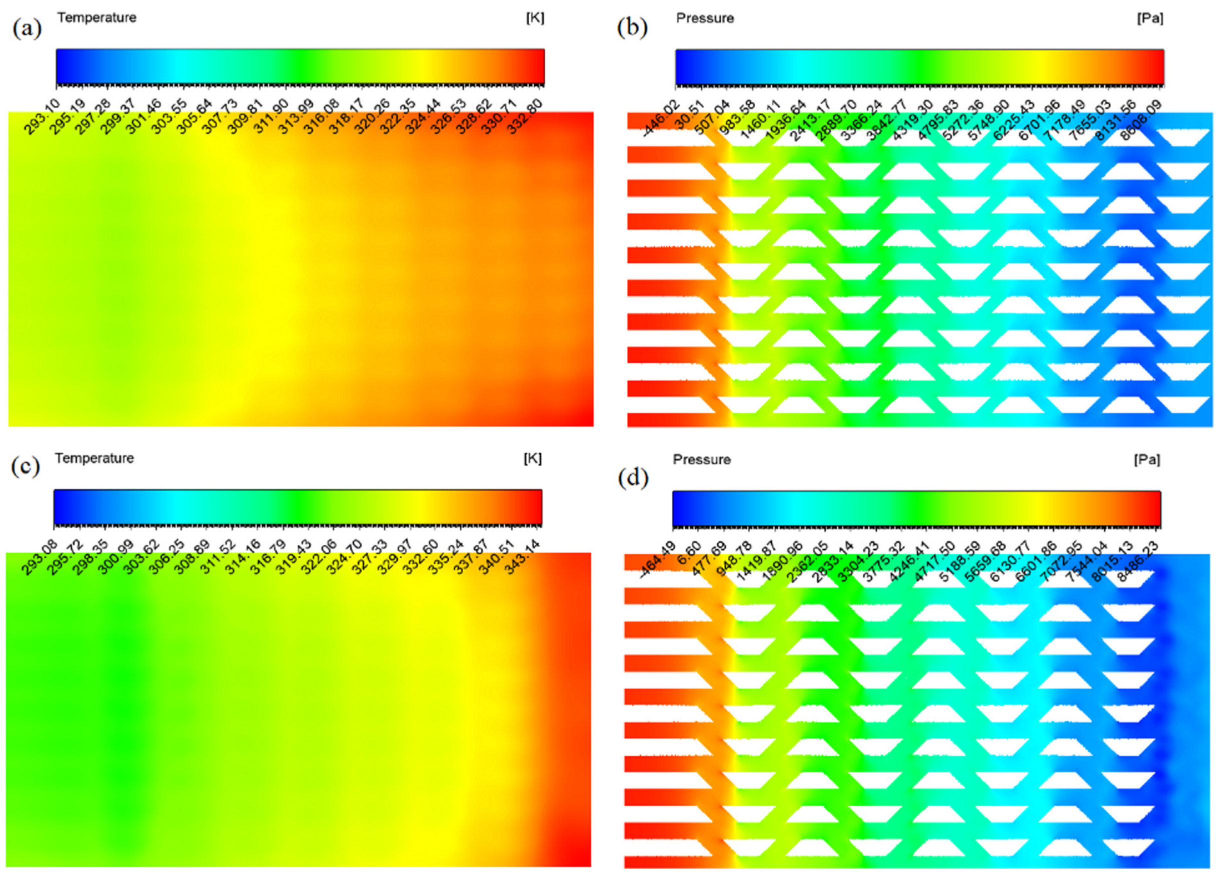

Fig. 5. (a) (c) Temperature distribution of the heat source; (b) (d) pressure distribution of the heat sink on x-y plane (z = 0.15 mm). (a) and (b) represent heat sink with $d_r = 1.0$, while (c) and (d) represent heat sink with $d_r = 1.5$.

$W_{wr} = 1.020$), which can illustrate the effect of d_r on the flow and heat transfer performance of the hybrid heat sink. Fig. 6 displays the temperature and pressure distribution contours for heat sinks with $W_{wr} = 0.5$ and $W_{wr} = 1.0$ when other design variables are kept constant ($d_r = 1.623$, $W_{1r} = 2.0$, $W_{cr} = 0.6$), which can illustrate the effect of W_{wr} on the flow and heat transfer performance of the hybrid heat sink. In addition, we define the relative differences of inlet pressure P_{in} and maximum temperature T_{max} between two contrastive heat sinks as follows:

$$\frac{\Delta T_{max1} - \Delta T_{max2}}{\Delta T_{max1}} = \frac{(T_{max1} - 293.15) \text{ - } (T_{max2} - 293.15)}{(T_{max1} - 293.15)}, \tag{7}$$

$$\frac{\Delta P_1 - \Delta P_2}{\Delta P_1} = \frac{P_{in1} - P_{in2}}{P_{in1}}. \tag{8}$$

The relative differences of P_{in} and T_{max} for heat sinks with $d_r = 1.0$ and $d_r = 1.5$ are -2.20% and 20.69% respectively. The relative differences of P_{in} and T_{max} for heat sinks with $W_{cr} = 0.5$ and $W_{wr} = 1.0$ are 23.45% and -5.84% respectively. The high-temperature regions of the two heat sinks appear at the edge of the outlet due to the continuous heat absorption of the coolant, while the high-pressure regions locate at the entrance region (Fig. 5). It is obvious that the maximum temperature T_{max} increases with increasing d_r, but there is almost no obvious change in pressure drop ΔP (i.e. P_{in}) between heat sinks with $d_r = 1.0$ and $d_r = 1.5$. The main reason for the different effects of d_r on P_{in} and T_{max} can be explained from the variation of flow velocity and streamlines distribution around secondary fins. As shown in Figs. 7(a) and (c), the maximum flow velocity is observed at the centre of the microchannel and the minimum value is located at fluid vortex. As pointed out in our previous work [42], the secondary channel has a dual effect on the pressure drop ΔP. On the one hand, it can increase ΔP by promoting fluid mixing. On the other hand, it can reduce ΔP by providing more flow area, which results in that the main influence factor on ΔP is the flow velocity in the main channel rather than the secondary channel. As can be seen in Figs. 7(a) and (c), no obvious differences of the flow velocity between heat sinks with $d_r = 1.0$ and $d_r = 1.5$ are observed. Therefore, the design variable d_r has limited influence on P_{in}. In terms of the maximum temperature T_{max}, larger d_r means larger secondary flow passage width d, which makes more coolant flow through the secondary channels. In addition, larger d_r brings larger vortex. The flow streamline distributions of heat sinks with $d_r = 1.0$ and $d_r = 1.5$ are shown in Figs. 7(b) and (d), respectively. It is obvious that heat sink with $d_r = 1.5$ has larger flow area. However, the high-temperature region locates at the outlet edge. Larger d_r brings larger secondary flow passage width d, which leads to no trapezoidal fin located at the edge of the outlet. Therefore, the maximum temperature T_{max} increases with increasing the relative secondary channel width d_r.

Similarly, the main reason for the different effects of W_{wr} on P_{in} and T_{max} can also be explained from the variation of flow velocity and streamlines distribution around secondary fins. Fig. 6 shows the high-temperature region of the heat sink with $W_{wr} = 0.5$ nears the edge of the outlet, but for heat sink with $W_{wr} = 1.0$ it locates at the bottom right edge due to the specific distribution of trapezoid fins. In addition, the high-pressure regions of the two heat sinks all locate at the entrance region. It is obvious that pressure drop ΔP (i.e. P_{in}) increases with increasing W_{wr}, but there is almost no obvious change in the maximum temperature T_{max} between heat sinks with $W_{wr} = 0.5$ and $W_{wr} = 1.0$. As shown in Figs. 8(a) and (c), smaller W_{wr} will reduce the channel wall W_w and brings more main channels, which leads to lower flow velocity. The water velocity of heat sink with $W_{wr} = 0.5$ is obviously lower than heat sink with $W_{wr} = 1.0$. Therefore, heat sink with $W_{wr} = 1.0$ has larger pressure drop ΔP (i.e. P_{in}). In terms of the maximum temperature

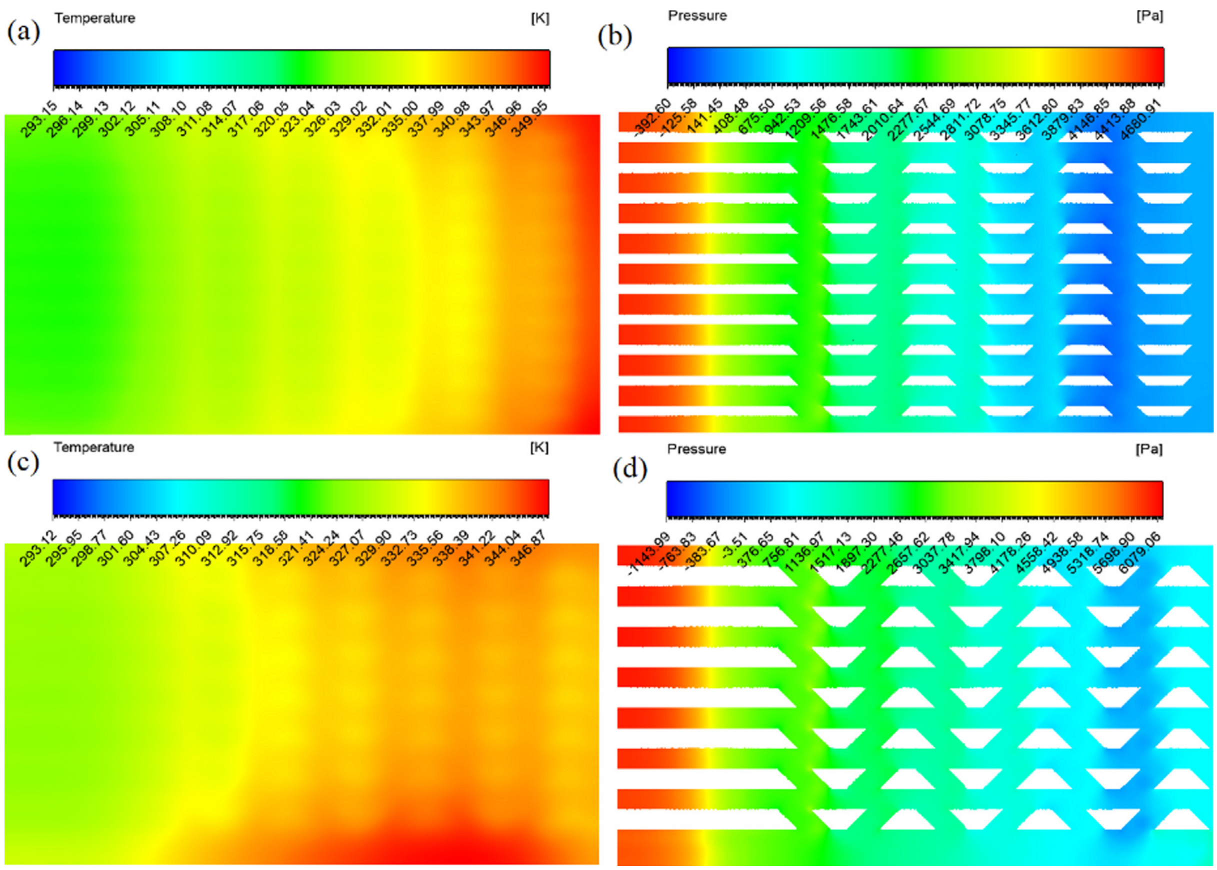

Fig. 6. (a) (c) Temperature distribution of the heat source; (b) (d) pressure distribution of the heat sink on x-y plane ($z = 0.15$ mm). (a) and (b) represent heat sink with $W_{wr} = 0.5$, while (c) and (d) represent heat sink with $W_{wr} = 1.0$.

T_{max}, larger W_{wr} means larger channel wall W_w, which may lead to no trapezoid fins located at the bottom right edge. Since T_{max} is significantly influenced by the distribution of secondary fins, heat sink with $W_{wr} = 1.0$ has almost the same T_{max} compared with heat sink with $W_{wr} = 0.5$.

4.2. Response surface model fitting and error analysis

The approximate functions must be constructed before invoking NSGA-II to generate Pareto-optimal solutions. A platform with response surface methodology and multi-objective genetic algorithm is established to construct the approximate functions and implement the subsequent optimization. 140 data points (see Appendix A) are randomly selected from the 160 data points to construct approximation model and the remaining data points (see Appendix B) are applied to test the availability of the model. A third-order polynomial surrogate functions of pumping power P_p and total thermal resistance R_t are represented as follows:

$$\begin{aligned} P_p = \; & 3.7452 + 0.0260W_{1r} - 12.9690W_{cr} - 0.6410W_{wr} + 0.1200W_{1r}^2 \\ & + 17.4837W_{cr}^2 + 2.9549W_{wr}^2 \\ & - 0.0736W_{1r}W_{cr} - 0.0871W_{1r}W_{wr} - 1.1882W_{cr}W_{wr} - 0.0358W_{1r}^3 \\ & - 7.5136W_{cr}^3 - 1.3348W_{wr}^3, \end{aligned} \tag{9}$$

$$\begin{aligned} R_t = \; & 0.6112 - 0.1032d_r + 0.1149W_{1r} + 0.1391W_{cr} \\ & + 0.0757\, d_r^2 - 0.1042W_{1r}^2 + 0.6367W_{cr}^2 \\ & + 0.0086d_rW_{1r} + 0.0399d_rW_{cr} - 0.0023W_{1r}W_{cr} - 0.0159d_r^3 \\ & + 0.0244W_{1r}^3 - 0.2489W_{cr}^3. \end{aligned} \tag{10}$$

Figs. 9(a) and (b) show the linear regression of the approximate models for pumping power P_p and total thermal resistance R_t, respectively. The R^2 values of P_p and R_t are calculated as 0.955 and 0.915, respectively, indicating that the prediction accuracy of the surrogate model has high reliability.

4.3. Optimization results and verification

The pumping power P_p and the total thermal resistance R_t are conflicting. Therefore, there is no single geometric parameter of the hybrid heat sink that yields the best design. Multi-objective optimization using NSGA-II is conducted by minimizing R_t and P_p simultaneously. The parameter settings of NSGA-II in this study are presented in Table 1. As shown in Fig. 10, a total of 2001 feasible solutions and 374 Pareto-optimal solutions are obtained by optimization. Those Pareto-optimal solutions resemble a concave front named Pareto frontier curve, which reveals a clear relation between the two conflicting objective functions. As R_t decreases, P_p will increase. Every solution of the Pareto-optimal solution represents one hybrid heat sink that there is no other scheme that is better than this one under the same working condition. Therefore, a designer can select the most appropriate one from Pareto-optimal solutions according to their limits or priorities. It should be noted that we can't judge which hybrid heat sink has better or worse temperature uniformity at the exit because the temperature uniformity isn't the optimization objective of this paper. But there is no doubt that the optimized hybrid heat sink has better temperature uniformity within the entire heat source than those without optimization. The numerical results of the simple MMC heat sink with $d_r = W_{1r} = W_{wr} = 1$ and $W_{cr} = 0.5$, at a flow rate of 0.08 L/min is also plotted in Fig. 10. The total thermal resistance and pumping power of the MMC heat sink are 0.8763 K/W and 0.01078 W, respectively. The corresponding four dimensionless geometric parameters d_r, W_{1r}, W_{cr}

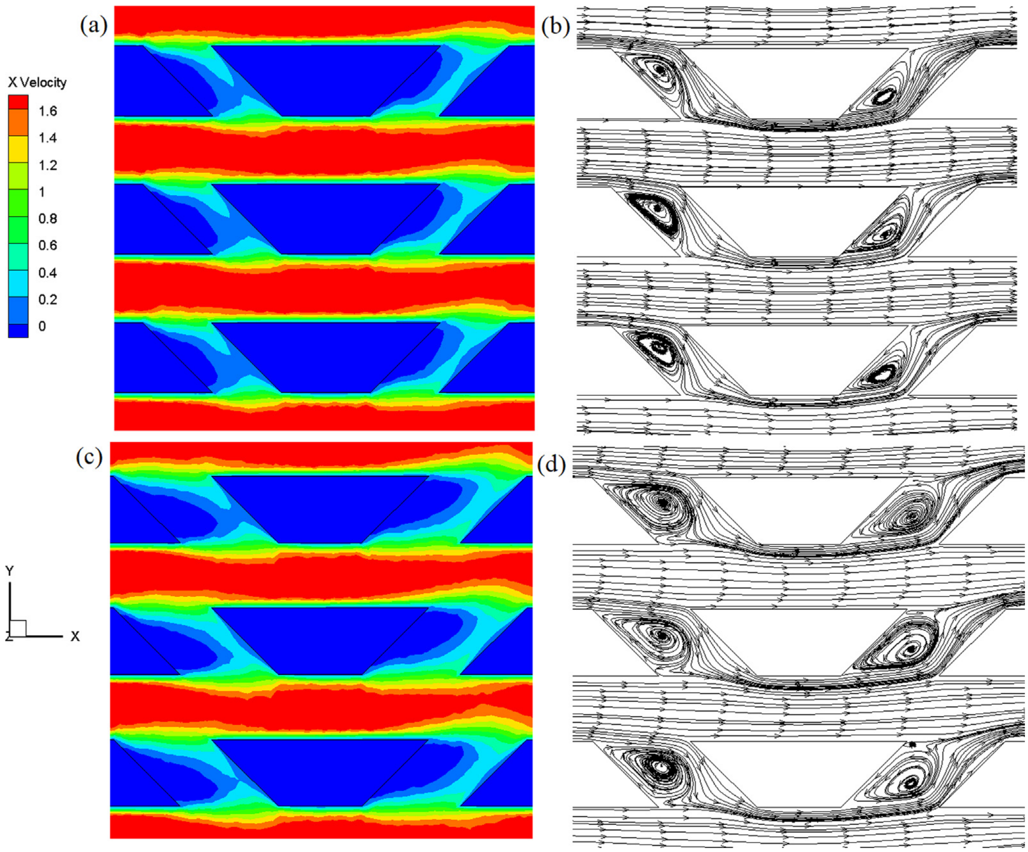

Fig. 7. (a) (c) Flow velocity distribution, (b) (d) streamlines distribution around secondary fins on x-y plane (z = 0.15 mm). (a) and (b) represent heat sink with d_r = 1.0, while (c) and (d) represent heat sink with d_r = 1.5.

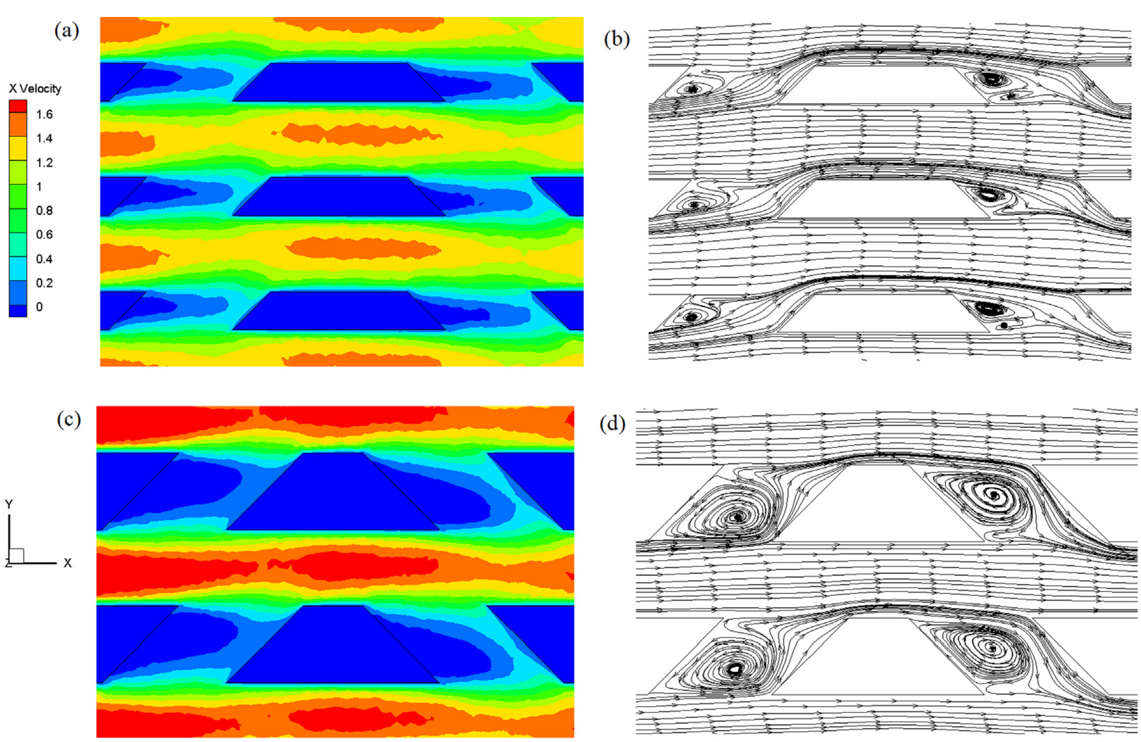

Fig. 8. (a) (c) Flow velocity distribution, (b) (d) streamlines distribution around secondary fins on x-y plane (z = 0.15 mm). (a) and (b) represent heat sink with W_{wr} = 0.5, while (c) and (d) represent heat sink with W_{wr} = 1.0.

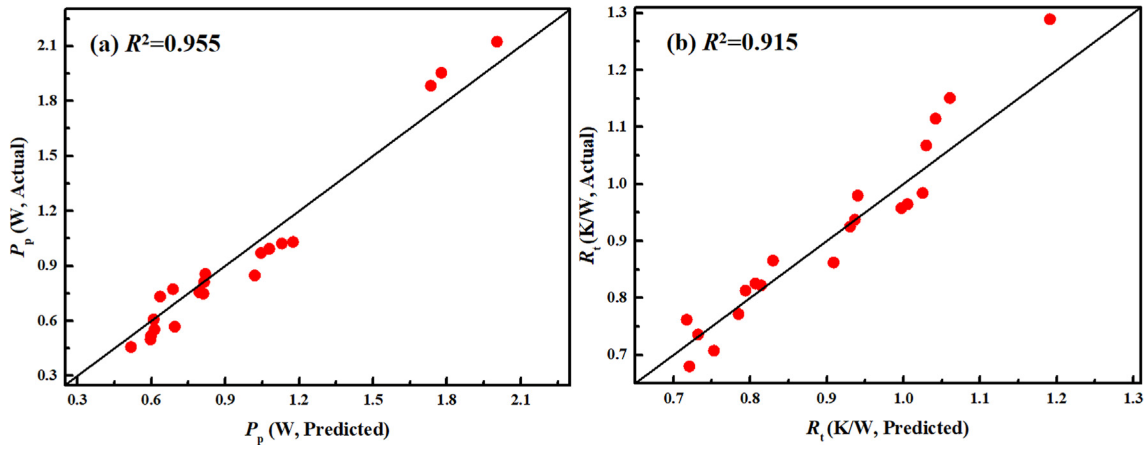

Fig. 9. Linear regression of the approximate models for (a) pumping power P_p and (b) total thermal resistance R_t.

Table 1
NSGA-II parameters in this study.

Parameters	Value
Population Size	20
Number of Generations	100
Crossover Probability	0.9
Crossover Distribution Index	10.0
Mutation Distribution Index	20.0

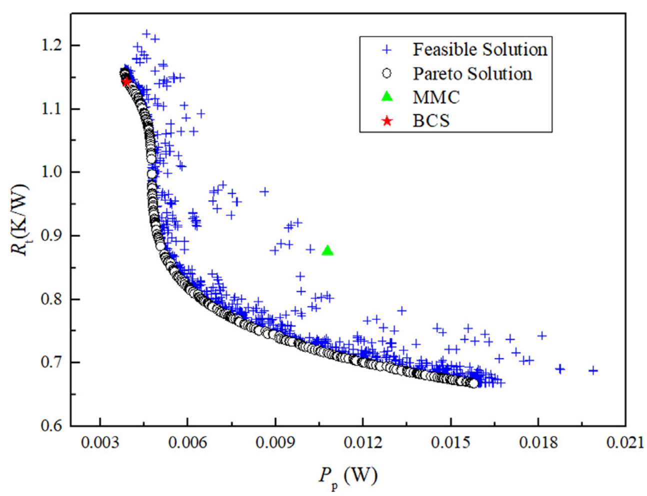

Fig. 10. The optimization results of the hybrid heat sink using NSGA-II.

and W_{wr} of the optimized hybrid heat sink with the same pumping of 0.01078 W are 0.817, 0.201, 0.34 and 0.5 and it's total thermal resistance is 0.7113 K/W, which is 18.83% lower than that of the MMC heat sink. Although the initial data sample points used in modeling and optimization are selected using the optimal Latin hypercube, it can ensure that the points taken in the design space are uniform and reasonable due to the excellent space filling property of the algorithm, which can ensure that the influence of the initial data sample points on the optimization results can be ignored.

In order to verify the optimization results, ten data points are randomly selected from Pareto-optimal solutions to compare with CFD results. The geometric parameters of those ten data points are extracted for computational fluid dynamic simulations. The pumping power P_p and total thermal resistance R_t getting from the optimization and numerical results are shown in Table 2. The relative deviations $E\%$ for P_p and R_t between them are calculated as

$$E\% = \frac{J_{CFD} - J_{Pre}}{J_{CFD}} \times 100, \tag{11}$$

where J denotes the value of thermal resistance or pumping power. Whether for P_p or R_t, the absolute relative deviations all less than 15%. In addition, the average value of the absolute relative deviations of those ten data points is also calculated. The average relative deviations of the pumping power and total thermal resistance are 7.90% and 7.75%, demonstrating that the convincing capability of the current mathematical model for generalization.

As mentioned above, the parametric modeling (UG), mesh generation (STAR-CCM+) and computational fluid dynamics calculation (ANSYS Fluent 14.0) are integrated by using a software platform. The designer can use this platform to obtain sample points with design parameters and corresponding optimization objectives automatically. Additionally, a platform with response surface methodology and multi-objective genetic algorithm is also established to construct response surface and implement the subsequent optimization. The optimization strategy has high efficiency and it will take about 160 h in total using a computer with quad-core Intel processor. Therefore, the entire optimization strategy is easy to use for designer in the practical design. In addition, it is also convenient to optimize the performance of other types of heat sinks using the optimization strategy with litter change on these two platforms.

4.4. Best compromise Pareto-front solution

In present study, we choose the TOPSIS method and information entropy weight to obtain the best compromise solution. The process of determining attribute weights is described below:

(1) Create the initial matrix $(r_{ij})_{k\times m}$ with k solutions and m objective

Table 2
Feasibility analysis of the optimization results.

Point	Prediction		CFD		E (%)	
	P_p (W)	R_t (K/W)	P_p (W)	R_t (K/W)	P_p	R_t
1	0.00384	1.15700	0.00431	1.05732	11.05	−9.43
2	0.00441	1.10284	0.00431	1.07657	−2.27	−2.44
3	0.00479	0.95950	0.00514	0.98846	6.97	2.93
4	0.00540	0.85233	0.00594	0.91711	9.09	7.06
5	0.00673	0.79168	0.00721	0.89172	6.63	11.22
6	0.00841	0.75121	0.00985	0.81655	14.61	8.00
7	0.01206	0.70051	0.01294	0.77125	6.85	9.17
8	0.01221	0.69951	0.01270	0.62474	3.91	−11.97
9	0.01483	0.67550	0.01660	0.72330	10.65	6.61
10	0.01577	0.66828	0.01696	0.73143	7.01	8.63

functions;

(2) Normalize the initial matrix by

$$t_{ij} = \frac{r_{ij}}{\sum_{i=1}^{k} r_{ij}}, \text{ where } \sum_{i=1}^{k} t_{ij} = 1; \tag{12}$$

(3) Calculate the information entropy E_j using

$$E_j = -\frac{1}{\ln k}\sum_{i=1}^{k}(r_{ij}\ln r_{ij}); \tag{13}$$

(4) The attribute weight w_j is defined as

$$W_j = \frac{1 - E_j}{\sum_{j=1}^{m}(1 - E_j)}. \tag{14}$$

The weights of the pumping power P_p and total thermal resistance R_t are 0.86 and 0.14 respectively. As shown in Fig. 10, the pentagram represents the obtained BCS based on TOPSIS and entropy method. The pumping power and total thermal resistance of the BCS are 0.00390 W and 1.14315 K/W respectively and the corresponding four dimensionless geometric parameters d_r, W_{1r}, W_{cr} and W_{wr} are respectively 0.455, 0.204, 1.0 and 0.5. The BCS is located near the minimum pumping power because that the pumping power has larger weight than total thermal resistance. However, it should be noted that there are many different approaches for determining the weights and the process of selecting the final optimal solution is mostly carried out based on engineering experiences and decision makers' priorities.

5. Conclusions

Multi-objective optimization of the hybrid microchannel heat sink combining manifold concept with secondary oblique channels (MMC-SOC) is performed. Four dimensionless geometric paraters, the relative secondary channel width d_r, relative longer-edge length W_{1r} of the fin under the inlet, relative channel width W_{cr} and relative channel wall width W_{wr} are selected as the design variables. The total thermal resistance R_t and pumping power P_p are simultaneously minimized at constant volume flow rate in the optimization process. The main conclusions are as follows:

1. A novel optimization approach, based on optimal Latin hypercube design, Pareto chart analysis, response surface methodology, the non-dominated sorting genetic algorithm II and technique for order preference by similarity ideal solution, has been proposed and applied to deal with the multi-objective optimization of the MMC-SOC heat sink. The optimization approach can also be applied to optimize the performance of other types of heat sinks;
2. 160 sample points are generated by the Opt LHD method. The Pareto chart analysis indicates that the design parameter d_r has a negligible effect on inlet pressure P_{in} and the design parameter W_{wr} has a negligible effect on the maximum temperature T_{max}. The temperature, pressure contours and the flow velocity, streamline distributions, visually show the effects of design variables d_r and W_{wr} on the objective functions;
3. RSM is used to generate approximate functions between the the objectives and design parameters, and NSGA-II is selected to minimize pumping power P_p and total thermal resistance R_t simultaneously. A total of 374 Pareto-optimal solutions are obtained and verified by CFD results. The hybrid heat sink shows superior performance compared with the original MMC design and can reduce R_t by 18.83% under the same P_p;
4. Furthermore, TOPSIS with entropy weight method is introduced to select the BCS from Pareto-optimal solutions. The BCS is located near the minimum pumping power because that the P_p has larger weight.

Declaration of Competing Interest

The authors declare that they have no known competing financial interests or personal relationships that could have appeared to influence the work reported in this paper.

Acknowledgement

This project was supported by the National Natural Science Foundation of China (Nos. 51825601, 51676108) and Science Fund for Creative Research Groups of China (No. 51621062).

Appendix A. Supplementary material

Supplementary data to this article can be found online at https://doi.org/10.1016/j.applthermaleng.2020.115592.

References

[1] G.E. Moore, Cramming more components onto integrated circuits, Electronics 38 (1965) 114–117.
[2] M.M. Waldrop, The chips are down for Moore's law, Nat. News. 530 (2016) 144–147, https://doi.org/10.1038/530144a.
[3] A.D. Franklin, Nanomaterials in transistors: From high-performance to thin-film applications, Science 349 (2015) aab2750, https://doi.org/10.1126/science.aab2750.
[4] A. Bar-Cohen, J.J. Maurer, J.G. Felbinger, DARPA's intra/interchip enhanced cooling (ICECool) program, in: Proceedings of the CS MANTECH Conference, New Orleans, Louisiana, 2013, pp. 171–174.
[5] L.L. Yuan, S. Liu, M.X. Chen, X.B. Luo, Thermal analysis of high power LED array packaging with microchannel cooler, in: 7th International Conference on Electronics Packaging Technology, Shanghai, 2006, pp. 574–577. https://doi.org/10.1109/ICEPT.2006.359826.
[6] X.H. Yang, S.C. Tan, Y.J. Ding, J. Liu, Flow and thermal modeling and optimization of micro/mini-channel heat sink, Appl. Therm. Eng. 117 (2017) 289–296, https://doi.org/10.1016/j.applthermaleng.2016.12.089.
[7] W. Qu, I. Mudawar, Experimental and numerical study of pressure drop and heat transfer in a single-phase micro-channel heat sink, Int. J. Heat Mass Transf. 45 (2002) 2549–2565, https://doi.org/10.1016/S0017-9310(01)00337-4.
[8] Y. Zhu, D.S. Antao, K.-H. Chu, S. Chen, T.J. Hendricks, T. Zhang, E.N. Wang, Surface Structure Enhanced Microchannel Flow Boiling, J. Heat Transfer. 138 (2016) 091501, https://doi.org/10.1115/1.4033497.
[9] M. Yang, B.Y. Cao, W. Wang, H.M. Yun, B.M. Chen, Experimental study on capillary filling in nanochannels, Chem. Phys. Lett. 662 (2016) 137–140, https://doi.org/10.1016/j.cplett.2016.09.016.
[10] X.L. Xie, Z.J. Liu, Y.L. He, W.Q. Tao, Numerical study of laminar heat transfer and pressure drop characteristics in a water-cooled minichannel heat sink, Appl. Therm. Eng. 29 (2009) 64–74, https://doi.org/10.1016/j.applthermaleng.2008.02.002.
[11] H.Y. Zhang, D. Pinjala, P.S. Teo, Thermal management of high power dissipation electronic packages: from air cooling to liquid cooling, in: Electron. Packag. Technol. 2003 5th Conf. (EPTC 2003), 2003, pp. 620–625. https://doi.org/10.1109/EPTC.2003.1271593.
[12] D.B. Tuckerman, R.F.W. Pease, High-Performance Heat Sinking for VLSI, IEEE Electron Device Lett. EDL-2 (1981) 126–129, https://doi.org/10.1109/EDL.1981.25367.
[13] G.L. Morini, Single-phase convective heat transfer in microchannels: a review of experimental results, Int. J. Therm. Sci. 43 (2004) 631–651, https://doi.org/10.1016/j.ijthermalsci.2004.01.003.
[14] X.F. Peng, G.P. Peterson, Convective heat transfer and flow friction for water flow in microchannel structures, Int. J. Heat Mass Transf. 39 (1996) 2599–2608, https://doi.org/10.1016/0017-9310(95)00327-4.
[15] T.M. Harms, M.J. Kazmierczak, F.M. Gerner, Developing convective heat transfer in deep rectangular microchannels, Int. J. Heat Fluid Flow 20 (1999) 149–157, https://doi.org/10.1016/S0142-727X(98)10055-3.
[16] Z.G. Li, X.L. Huai, Y.J. Tao, H.Z. Chen, Effects of thermal property variations on the liquid flow and heat transfer in microchannel heat sinks, Appl. Therm. Eng. 27 (2007) 2803–2814, https://doi.org/10.1016/j.applthermaleng.2007.02.007.
[17] M.I. Hasan, A.A. Rageba, M. Yaghoubib, H. Homayoni, Influence of channel geometry on the performance of a counter flow microchannel heat exchanger, Int. J. Therm. Sci. 48 (2009) 1607–1618, https://doi.org/10.1016/j.ijthermalsci.2009.01.004.
[18] S.G. Kandlikar, S. Colin, Y. Peles, S. Garimella, R.F. Pease, J.J. Brandner, D.B. Tuckerman, Heat transfer in microchannels—2012 status and research needs, Trans. ASME J. Heat Transfer 135 (2013) 091001, https://doi.org/10.1115/1.4024354.
[19] S.N. Li, H.N. Zhang, J.P. Cheng, X.B. Li, W.H. Cai, Z.Y. Li, F.C. Li, A state-of-the-art

overview on the developing trend of heat transfer enhancement by single-phase flow at micro scale, Int. J. Heat Mass Transf. 143 (2019) 118476, https://doi.org/10.1016/j.ijheatmasstransfer.2019.118476.
[20] Y. Sui, C.J. Teo, P.S. Lee, Y.T. Chew, C. Shu, Fluid flow and heat transfer in wavy microchannels, Int. J. Heat Mass Transf. 53 (2010) 2760–2772, https://doi.org/10.1016/j.ijheatmasstransfer.2010.02.022.
[21] H.A. Mohammed, P. Gunnasegaran, N.H. Shuaib, Numerical simulation of heat transfer enhancement in wavy microchannel heat sink, Int. Commun. Heat Mass Transf. 38 (2011) 63–68, https://doi.org/10.1016/j.icheatmasstransfer.2010.09.012.
[22] Y.T. Yang, H.S. Peng, Numerical study of pin-fin heat sink with un-uniform fin height design, Int. J. Heat Mass Transf. 51 (2008) 4788–4796, https://doi.org/10.1016/j.ijheatmasstransfer.2008.02.017.
[23] S. Ndao, Y. Peles, M.K. Jensen, Multi-objective thermal design optimization and comparative analysis of electronics cooling technologies, Int. J. Heat Mass Transf. 52 (2009) 4317–4326, https://doi.org/10.1016/j.ijheatmasstransfer.2009.03.069.
[24] J. Yang, L. Li, L. Yang, J. Li, Uniform design for the parameters optimization of pin-fins channel heat sink, Appl. Therm. Eng. 120 (2017) 289–297, https://doi.org/10.1016/j.applthermaleng.2017.03.122.
[25] D. Yang, Z. Jin, Y. Wang, G. Ding, G. Wang, Heat removal capacity of laminar coolant flow in a micro channel heat sink with different pin fins, Int. J. Heat Mass Transf. 113 (2017) 366–372, https://doi.org/10.1016/j.ijheatmasstransfer.2017.05.106.
[26] F. Zhou, W. Zhou, Q. Qiu, W. Yu, X. Chu, Investigation of fluid flow and heat transfer characteristics of parallel flow double-layer microchannel heat exchanger, Appl. Therm. Eng. 137 (2018) 616–631, https://doi.org/10.1016/j.applthermaleng.2018.03.069.
[27] C. Leng, X.D. Wang, T.H. Wang, W.M. Yan, Multi-parameter optimization of flow and heat transfer for a novel double-layered microchannel heat sink, Int. J. Heat Mass Transf. 84 (2015) 359–369, https://doi.org/10.1016/j.ijheatmasstransfer.2015.01.040.
[28] G.M. Harpole, J.E. Eninger, Micro-channel heat exchanger optimization, in: Semicond. Therm. Meas. Manag. Symp. 1991. SEMI-THERM VII. Proceedings., Seventh Annu. IEEE. IEEE., 1991, pp. 59–63. https://doi.org/10.1109/STHERM.1991.152913.
[29] D. Copelandl, M. Behniaz, W. Nakayamal, Manifold microchannel heat sinks: isothermal analysis, IEEE Trans. on Compon. Packag. Manuf. Technology-Part A 20 (1997) 96–102, https://doi.org/10.1109/ITHERM.1996.534570.
[30] J.H. Ryu, D.H. Choi, S.J. Kim, Three-dimensional numerical optimization of a manifold microchannel heat sink, Int. J. Heat Mass Transf. 46 (2003) 1553–1562, https://doi.org/10.1016/S0017-9310(02)00443-X.
[31] E. Kermani, S. Dessiatoun, A. Shooshtari, M.M. Ohadi, Experimental investigation of heat transfer performance of a manifold microchannel heat sink for cooling of concentrated solar cells, in: Electron. Components Technol. Conf. 2009. ECTC 2009. 59th, 2009, pp. 453–459. https://doi.org/10.1109/ECTC.2009.5074053.
[32] S. Sarangi, K.K. Bodla, S.V. Garimella, J.Y. Murthy, Manifold microchannel heat sink design using optimization under uncertainty, Int. J. Heat Mass Transf. 69 (2014) 92–105, https://doi.org/10.1016/j.ijheatmasstransfer.2013.09.067.
[33] M.A. Arie, A.H. Shooshtari, S.V. Dessiatoun, E. Al-Hajri, M.M. Ohadi, Numerical modeling and thermal optimization of a single-phase flow manifold-microchannel plate heat exchanger, Int. J. Heat Mass Transf. 81 (2015) 478–489, https://doi.org/10.1016/j.ijheatmasstransfer.2014.10.022.
[34] S.N. Li, H.N. Zhang, X. Bin Li, Q. Li, F.C. Li, S. Qian, S.W. Joo, Numerical study on the heat transfer performance of non-Newtonian fluid flow in a manifold microchannel heat sink, Appl. Therm. Eng. 115 (2017) 1213–1225, https://doi.org/10.1016/j.applthermaleng.2016.10.047.
[35] K.P. Drummond, D. Back, M.D. Sinanis, D.B. Janes, D. Peroulis, J.A. Weibel, S.V. Garimella, A hierarchical manifold microchannel heat sink array for high-heat-flux two-phase cooling of electronics, Int. J. Heat Mass Transf. 117 (2018) 319–330, https://doi.org/10.1016/j.ijheatmasstransfer.2017.10.015.
[36] M.E. Steinke, S.G. Kandlikar, Single-Phase Heat Transfer Enhancement Techniques in Microchannel and Minichannel Flows, in: ASME 2nd Int. Conf. Microchannels Minichannels, 2004, pp. 141–148. https://doi.org/10.1115/ICMM2004-2328.
[37] Y.J. Lee, P.S. Lee, S.K. Chou, Enhanced microchannel heat sinks using oblique fins, in: ASME 2009 InterPack Conf. 2, 2009, pp. 253–260. https://doi.org/10.1115/InterPACK2009-89059.
[38] N.R. Kuppusamy, R. Saidur, N.N.N. Ghazali, H.A. Mohammed, Numerical study of thermal enhancement in micro channel heat sink with secondary flow, Int. J. Heat Mass Transf. 78 (2014) 216–223, https://doi.org/10.1016/j.ijheatmasstransfer.2014.06.072.
[39] I.A. Ghani, N.A.C. Sidik, R. Mamat, G. Najafi, T.L. Ken, Y. Asako, W.M.A.A. Japar, Heat transfer enhancement in microchannel heat sink using hybrid technique of ribs and secondary channels, Int. J. Heat Mass Transf. 114 (2017) 640–655, https://doi.org/10.1016/j.ijheatmasstransfer.2014.06.072.
[40] Z.Y. Guo, D.Y. Li, B.X. Wang, A novel concept for convective heat transfer enhancement, Int. J. Heat Mass Transf. 41 (1998) 2221–2225, https://doi.org/10.1016/S0017-9310(97)00272-X.
[41] Z.Y. Guo, W.Q. Tao, R.K. Shah, The field synergy (coordination) principle and its applications in enhancing single phase convective heat transfer, Int. J. Heat Mass Transf. 48 (2005) 1797–1807, https://doi.org/10.1016/j.ijheatmasstransfer.2004.11.007.
[42] M. Yang, B.Y. Cao, Numerical study on flow and heat transfer of a hybrid microchannel cooling scheme using manifold arrangement and secondary channels, Appl. Therm. Eng. 113896 (2019), https://doi.org/10.1016/j.applthermaleng.2019.113896.
[43] A. Husain, K.Y. Kim, Enhanced multi-objective optimization of a microchannel heat sink through evolutionary algorithm coupled with multiple surrogate models, Appl. Therm. Eng. 30 (2010) 1683–1691, https://doi.org/10.1016/j.applthermaleng.2010.03.027.
[44] Y. Wang, Y.L. He, D.H. Mei, W.Q. Tao, Optimization design of slotted fin by numerical simulation coupled with genetic algorithm, Appl. Energy 88 (2011) 4441–4450, https://doi.org/10.1016/j.apenergy.2011.05.030.
[45] G.D. Xia, Y.T. Jia, Y.F. Li, D.D. Ma, B. Cai, Numerical simulation and multiobjective optimization of a microchannel heat sink with arc-shaped grooves and ribs, Numer. Heat Tranf. A-Appl. 70 (2016) 1041–1055, https://doi.org/10.1080/10407782.2016.1230394.
[46] X.J. Shi, S. Li, Y.J. Mu, B.T. Yin, Geometry parameters optimization for a microchannel heat sink with secondary flow channel, Int. Commun. Heat Mass Transf. 104 (2019) 89–100, https://doi.org/10.1016/j.icheatmasstransfer.2019.03.009.
[47] R. Jin, W. Chen, A. Sudjianto, An efficient algorithm for constructing optimal design of computer experiments, J. Stat. Plan. Infer. 134 (2005) 268–287, https://doi.org/10.1016/j.jspi.2004.02.014.
[48] G.E. Box, K.B. Wilson, On the experimental attainment of optimum conditions, J. Roy. Stat. Soc. B 13 (1951) 1–38, https://doi.org/10.1111/j.2517-6161.1951.tb00067.x.
[49] J. Wen, K. Li, X. Zhang, C.L. Wang, S.M. Wang, J.Y. Tu, Optimization investigation on configuration parameters of serrated fin in plate-fin heat exchanger based on fluid structure interaction analysis, Int. J. Heat Mass Transf. 119 (2018) 282–294, https://doi.org/10.1016/j.ijheatmasstransfer.2017.11.058.
[50] K. Deb, A. Pratap, S. Agarwal, T. Meyarivan, A fast and elitist multiobjective genetic algorithm: NSGA-II, IEEE Trans. Evol. Comput. 6 (2002) 182–197, https://doi.org/10.1109/4235.996017.
[51] Y.J. Lai, T.Y. Liu, C.L. Hwang, Topsis for MODM, Eur. J. Oper. Res. 76 (1994) 486–500, https://doi.org/10.1016/0377-2217(94)90282-8.